

Interferometric Mapping of Magnetic Fields in Star-forming Regions III. Dust and CO polarization in DR21(OH)

Shih-Ping Lai¹, José M. Girart², and Richard M. Crutcher

*Astronomy Department, University of Illinois, 1002 W. Green Street, Urbana, IL 61801;
slai@astro.umd.edu, jgirart@am.ub.es, crutcher@astro.uiuc.edu*

ABSTRACT

We present the polarization detections in DR21(OH) from both the thermal dust emission at 1.3 mm and the CO $J=2\rightarrow 1$ line obtained with the Berkeley-Illinois-Maryland Association (BIMA) array. Our results are consistent with the prediction of the Goldreich-Kylafis effect that the CO polarization is either parallel or perpendicular to the magnetic field direction. The detection of the polarized CO emission is over a more extended region than the dust polarization, while the dust polarization provides an aide in resolving the ambiguity of the CO polarization. The combined results suggest that the magnetic field direction in DR21(OH) is parallel to the CO polarization and therefore parallel to the major axis of DR21(OH). The strong correlation between the CO and dust polarization suggests that magnetic fields are remarkably uniform throughout the envelope and the cores. The dispersion in polarization position angles implies a magnetic field strength in the plane of the sky of about 1 mG, compared with about 0.5 mG inferred for the line-of-sight field from previous CN Zeeman observations. Our CO data also show that both MM1 and MM2 power high-velocity outflows with $v \gtrsim 25$ km s⁻¹ relative to the systematic velocity.

1. Introduction

In order to study the importance of the magnetic field in the star formation process, it is essential to obtain high resolution maps of magnetic fields in dense molecular cores where stars form. Mapping polarized thermal dust emission has been the most successful

¹Current address: Department of Astronomy, University of Maryland, College Park, MD 20742-2421

²Current address: Departament d'Astronomia i Meteorologia, Universitat de Barcelona, 08028 Barcelona, Catalunya, Spain

technique to explore the magnetic field morphology in dense cores (Greaves et al. 1999a; Dotson et al. 2000; Ward-Thompson et al. 2000; Matthews & Wilson 2002). In general, the magnetic field direction is perpendicular to the dust polarization direction. Using the BIMA millimeter interferometer, we have obtained high resolution maps of dust polarization in several star-forming cores (Rao et al. 1998; Girart, Crutcher, & Rao 1999; Lai et al. 2001, hereafter Paper I; Lai et al. 2002, hereafter Paper II). Our results show that the magnetic fields in these cores are remarkably uniform, suggesting that magnetic fields are relatively strong and cannot be ignored in cloud evolution and star formation.

Polarization arising from the spectral line emission, via the Goldreich-Kylafis effect, provides an opportunity to probe the magnetic field directions in the regions where the dust emission is too weak for polarization detections. This effect predicts that the line polarization has a direction either perpendicular or parallel to the magnetic field direction, depending on the relative angles between the magnetic field, the velocity gradient, and the line of sight (Goldreich & Kylafis 1981, 1982; Kylafis 1983). Detection of this effect requires high sensitivity and spatial resolution in order to separate regions with different physical conditions; therefore, the observational confirmation of this effect comes very recently (Greaves et al. 1999b; Girart, Crutcher, & Rao 1999). Here we present another example, DR21(OH), with polarization detections in both the dust emission and in the CO $J=2\rightarrow 1$ line. Simultaneous observations of both effects help us to extend the mapping area of the magnetic field and to resolve the ambiguity of the predicted field direction from the CO polarization.

DR21(OH), also known as W75S or W75S-OH, is located $3'$ north of the H II region DR21 in the Cygnus X molecular cloud/H II region complex (Harvey et al. 1986; Downes & Rinehart 1966). The distance to DR21(OH) is commonly assumed to be 3 kpc, although the value is very uncertain (Campbell et al. 1982). Its association with masers of OH (Norris et al. 1982), H₂O (Genzel & Downes 1977), and CH₃OH (Batra & Menten 1988; Plambeck & Menten 1990) suggests the presence of high-mass, young stellar objects. The main component of DR21(OH) has been resolved into two compact cores, MM1 and MM2 (Woody et al. 1989), with a total mass of $\sim 100 M_{\odot}$ in roughly virial equilibrium (Padin et al. 1989). The Zeeman splitting in CN lines, which trace high density of $n_{H_2} \sim 10^5 - 10^6 \text{ cm}^{-3}$, has been detected in both cores. In fact, MM1 and MM2 are two of the three cores in which the Zeeman effect in CN lines has been detected to date. The line-of-sight magnetic field strength, B_{los} , was determined to be -0.4 mG for MM1 and -0.7 mG for MM2 (Crutcher et al. 1999). Therefore, by mapping magnetic field directions in the plane of sky from dust and CO polarization, we have an opportunity to explore the magnetic field of DR21(OH) in 3-dimensional space.

2. Observations and Data Reduction

The observations were carried out from 1999 December to 2000 May using nine BIMA antennas with 1-mm Superconductor-Insulator-Superconductor (SIS) receivers and quarter-wave plates. The digital correlator was set up to observe both continuum and the CO $J=2\rightarrow1$ line simultaneously. The continuum was observed with a 750 MHz window centered at 226.9 GHz in the lower sideband and a 700 MHz window centered at 230.9 GHz in the upper sideband. An additional 50 MHz window in the upper sideband was set up to observe the CO $J=2\rightarrow1$ line. The primary beam was $\sim 50''$ at 1.3 mm wavelength. Data were obtained in the C and D array configurations, and the projected baseline ranges were 5–68 and 4.5–20 kilowavelengths. The on-source integration time in the C and D array was 23.1 and 2.7 hours, respectively.

The BIMA polarimeter and the calibration procedure are described in detail in Paper I. The average instrumental polarization of each antenna, which was removed from the DR21(OH) data by our standard calibration procedure, was $6.2\% \pm 0.5\%$ for our observations. The dust continuum images of Stokes I , Q , and U were made with natural weighting and the resulting synthesized beam is $3''.9 \times 3''.5$ (PA= 12°). The CO images were made with a Gaussian taper applied to the CO visibilities in order to increase the sensitivity per beam, and the synthesized beam for CO is $5''.7 \times 4''.6$ with PA= -7° . These maps were binned to approximately half-beamwidth per pixel ($2''.0 \times 1''.6$) to reduce oversampling in our statistics. The binned maps were then combined to obtain the linearly polarized intensity (I_p), the position angle (ϕ), and the polarization percentage (p), along with their uncertainties as described in Section 2 of Paper I. When weighted with I_p , the average measurement uncertainty in the position angle for our observations was $7.6 \pm 1.2^\circ$.

3. Results

Figure 1 shows the dust continuum in contours and the CO $J=2\rightarrow1$ emission (v_{LSR} of -10 km s^{-1} , $\Delta v = 11.5 \text{ km s}^{-1}$) in grey scale overlaid with polarization vectors of dust and CO. The CO emission in Figure 1 is only integrated over the velocity range associated with the polarization detections. The dust polarization vectors are plotted at positions where the linearly polarized intensity I_p is greater than $3\sigma_{I_p}$ ($1\sigma_{I_p} = 2.0 \text{ mJy beam}^{-1}$) and the total intensity I is greater than $3\sigma_I$ ($1\sigma_I = 4.0 \text{ mJy beam}^{-1}$). The CO polarization vectors are shown at positions with the linearly polarized intensity greater than $3\sigma_{I_p}$ ($1\sigma_{I_p} = 29 \text{ mJy beam}^{-1}$) and the integrated intensity greater than $30\sigma_I$ ($1\sigma_I = 0.13 \text{ Jy beam}^{-1}$). The total area with polarization detections is ~ 6 beam sizes for dust and ~ 7 beam sizes for CO. Table 1 lists the dust and CO polarization vectors shown in Figure 1. The separation

between vectors is approximately half of the synthesized beam.

3.1. Dust Emission and Polarization

DR21(OH) is comprised of two continuum sources, MM1 in the east and MM2 in the west (Fig. 1). Both sources are resolved, and their sizes are $6''.5 \times 5''.2$ (PA= 30°) for MM1 and $7''.4 \times 6''.6$ (PA= 15°) for MM2. The physical sizes are ~ 0.1 pc at a distance of 3 kpc. MM1 and MM2 each has a flux of 1.6 Jy. Since the free-free emission in these two cores is negligible (Johnston, Henkle, & Wilson 1984), the continuum flux of DR21(OH) at 1.3 mm is dominated by the dust emission.

The polarization detections in the dust continuum of DR21(OH) appear in several scattered positions. Figure 2(a) shows that the distribution of the polarization angles in the dust continuum of DR21(OH); the average angle is -38° and the dispersion is $28^\circ \pm 9^\circ$. This large dispersion includes the dispersion caused by the turbulent motions as well as the variation of the magnetic field structure across the double cores. For further examination, we divide the polarization detections into three groups according to their spatial locations, which are near MM1, MM2, and the northern edge of DR21(OH). The histograms of the polarization angles in these three groups are shown separately in Figure 2(b)-(d). The polarization emission associated with MM1 appears in two sub-groups with distinct polarization angles: one in the northeast side of the MM1 peak with polarization angles at $-10^\circ \pm 2^\circ$, and the other in the southern part of MM1 with polarization angles at $-50^\circ \pm 7^\circ$. The vectors associated with MM2 show more continuous change between -35° to 15° with an average of $-18^\circ \pm 12^\circ$. The vectors in the northern edge have position angles at $-86^\circ \pm 12^\circ$, which are very different from those associated with MM1 and MM2. We discuss the four possibilities for the difference between the northern edge and the two main cores in §4.3. Overall, although we cannot completely decouple the variation of the magnetic field structure from the angle dispersion, we may use the dispersion of MM1 and MM2 ($21^\circ \pm 7^\circ$) as the upper limit of the angle dispersion associated with the turbulent motions in the dust cores.

The distributions of the polarization percentage versus the total intensity and the distance to the peaks of MM1 and MM2 are plotted in Figure 3. Fig. 3(a) shows that the polarization percentage decreases toward regions of high intensity. The least-squares fit on $\log_{10} p$ versus $\log_{10} I$ for all data points gives $\log_{10} p = (-2.08 \pm 0.01) - (0.95 \pm 0.01) \times \log_{10} I$ with a correlation coefficient of -0.98 . Fig. 3(b) and (c) show that the polarization percentage decreases toward the center of both cores. Because higher intensity and smaller radius both imply higher density, our results suggest that the polarization percentage decreases toward high density regions. This is consistent with what we have observed in W51 e1/e2

and NGC 2024 FIR 5 (Paper I and II), and we again attribute this to the decrease of the dust polarization efficiency toward high density regions.

3.2. CO $J=2\rightarrow1$ Emission and Polarization

Figure 4 shows the Stokes I , Q , and U spectra of CO $J=2\rightarrow1$ emission integrated over the region associated with the polarization peak in the center of the dust continuum (the region is shown with a dashed rectangle in Figure 1). The CO line is clearly optically thick and contains emission from both the dense core and the ambient gas, resulting in a wide linewidth in Stokes I . The Stokes I line profile shows two peaks at $v_{LSR} \sim -10$ and 0 km s $^{-1}$ with a minimum at -4 km s $^{-1}$. The velocities of these peaks are different from previous CS and CN observations, which are at $v_{LSR} \sim -5$ and -1 km s $^{-1}$ (Richardson et al. 1994; Crutcher et al. 1999). Therefore, the dip in the Stokes I line profile should be due to self-absorption and/or severe missing flux.

The CO polarized flux is mostly associated with the -10 km s $^{-1}$ peak in the spectrum (Fig. 4). The polarization map of this peak is shown in Fig. 1. The detection of the polarized CO emission is over a more extended region than the dust polarization. Most of the polarized emission arises from a region associated with the dust continuum. We refer to this region as CO pol Main. The polarization angles in CO pol Main appear to decrease from east to west from 140° to 40° with an average of $89^\circ \pm 23^\circ$. There is also a polarized region with an area ~ 1 – 2 beamsizes at $\sim 15''$ northwest of the MM2 peak, which we refer to CO pol West. The average polarization angle in CO pol West is $59^\circ \pm 10^\circ$. The polarized flux drops to zero between CO pol Main and CO pol West, suggesting there is significant change in the field geometry between these two regions.

3.3. Comparison between Dust and CO Polarization

Figure 5 shows the distribution of the CO polarization angles in CO pol Main and Figure 6 shows the distribution of the difference between the polarization angles of CO and dust ($\phi_{CO} - \phi_{dust}$) for those positions in which detections have been made in both CO and dust emission. The Goldreich-Kylafis effect predicts that the CO polarization direction is either parallel or perpendicular to the magnetic field direction. Therefore, in theory $\phi_{CO} - \phi_{dust}$ should be either 0° or 90° . Our results are consistent with the theoretical predictions: near the northern edge, ϕ_{CO} is approximately parallel to ϕ_{dust} ; near the MM1 and MM2 cores, the CO polarization vectors are close to perpendicular to the dust polarization vectors with

average $\phi_{CO} - \phi_{dust} = 95^\circ$ and a dispersion of $31^\circ \pm 16^\circ$. If there is no correlation between the CO and dust polarization, the expected $\phi_{CO} - \phi_{dust}$ distribution would be flat because the chance for any angle difference are equal. The large dispersion could be explained by the combination of the intrinsic dispersion in dust and CO polarization (see Table 2), which is $30^\circ \pm 8^\circ$. Alternatively, it could be due to the fact that CO and dust do not trace exactly the same region, as the CO is optically thick and the dust emission is optically thin at 1mm. The strong correlation between the CO and dust polarization suggests that magnetic fields are remarkably uniform throughout the envelope and the cores.

3.4. High-velocity CO outflows

The existence of the high velocity gas in DR21(OH) has been suggested by Fischer et al. (1985) and Richardson et al. (1994) with high-velocity wings in the CO and CS line profiles. Our CO data provide the first map of the spectacular outflows in DR21(OH) (Fig. 7). The blue and red lobes shown in Fig. 7 are obtained by integrating over 7 km s^{-1} bandwidths centered at -30 km s^{-1} and 20 km s^{-1} , which are near the two ends of our correlator window. There are other possible outflow features at lower velocities; however, the CO emission suffers from the missing flux problem. The outflows could extend to higher velocities, as the intensity in the two end channels are still well above the rms noise (Fig. 4). Therefore, Fig. 7 only presents a partial picture of the outflows in DR21(OH).

Nevertheless, from the morphologies of the CO gas with $v \lesssim 25 \text{ km s}^{-1}$ relative to the systematic velocity, it seems that MM1 and MM2 each power high-velocity bipolar outflows. The northwestern blue lobe and the southeastern red lobe likely originate from MM2. Shock excited methanol masers appear aligned with these two lobes and MM2 (Plambeck & Menten 1990). The southwestern blue lobe and the northeastern red lobe could originate from both MM1 and MM2. In this picture the overlapped red and blue emission between MM1 and MM2 arises from the two outflow sources. Alternatively, the morphology could suggest a single bipolar outflow with a cone-like morphology, and with the CO lobes tracing the limb brightened region of the outflow. In principle, this hypothesis can be examined with the position-velocity diagram along the jet axis (Lee et al. 2000); however, the combination of the lack of extended emission and the possible complexity of the sources impede the diagnostic. MM1 and MM2 are both massive enough to contain multiple young stellar objects. In fact, MM2 has been resolved into two NH_3 cores with VLA observations (Mangum, Wootten, & Mundy 1992). On the other hand, the fact that the maser spots are either in or near the outflow lobes (Fig. 7), but not between the lobes, seems to favor the idea that these lobes are individual outflows. Further single-dish observations as well as higher resolution

observations would help to understand the driving sources and the kinematics of the outflows in DR21(OH).

4. Discussion

4.1. Magnetic Field Morphology

We attempt to construct the magnetic field morphology in DR21(OH) using both dust and CO polarization results. The dust polarization is perpendicular to the average field direction along the line of sight, if produced by magnetic alignment. The CO polarization angles could be either parallel or perpendicular to the field, according to the Goldreich-Kylafis effect.

Our CO polarization map in DR21(OH) shows that CO polarization provides measurements for the field structure in a more extended region than the dust polarization. Our dust polarization results suggest that the magnetic field directions are parallel to the CO polarization vectors in the south of the MM1 and MM2 peaks. But in the region to the northern edge where dust polarization is detected, the position angle of dust polarization has changed by about 90° . This could suggest that the magnetic field direction is perpendicular to the CO polarization in the northern region; however, it seems unlikely that the CO polarization traces such an abrupt change in the field direction, but still shows smooth variation in polarization angles from south to north. Although the dust polarization detections in the northern edge are marginal (Table 1), they have polarization angles perfectly consistent with the CO polarization, suggesting that they are probably not spurious. The unusual behavior of the dust polarization in the northern portion of the cores will be discussed in §4.3. Here we conclude that the field morphology in DR21(OH) is better represented by the CO polarization directions, which is approximately along the major axis of DR21(OH). Therefore, MM1 and MM2 are likely to be two condensations in a magnetic flux tube.

4.2. Magnetic Field Strengths and Directions

We use our measurements of polarization angle dispersion and the Zeeman measurements from Crutcher et al. (1999) to estimate the magnetic field strength and direction of DR21(OH). As discussed in Paper I and Paper II, the Chandrasekhar-Fermi (CF) equation with a correction factor of 0.5 may be used to estimate the plane-of-sky magnetic field strength (B_p). The measurements of the polarization angle dispersion associated with Alfvénic motion ($\delta\phi$), the dispersion of the turbulent linewidth, and the average density of

the core are needed for this estimate. There are two effects that could bias the measured $\delta\phi$ from its actual value: First, the contribution due to bending of the uniform magnetic field has not been taken out, which would increase $\delta\phi$. Second, any smoothing of the polarization morphology due to inadequate angular resolution would reduce $\delta\phi$. Since it is difficult to exclude these two factors in $\delta\phi$, we simply use $\delta\phi \sim 22^\circ$ of CO pol Main as an estimate (Table 2). The linewidth and density of DR21(OH) are adopted from Crutcher et al. (1999): the FWHM of CN is 2.3 km s^{-1} toward both cores and the density is 10^6 cm^{-3} for MM1 and $2 \times 10^6 \text{ cm}^{-3}$ for MM2. Therefore, the derived B_p is $\sim 0.9 \text{ mG}$ for MM1 and $\sim 1.3 \text{ mG}$ for MM2. It is interesting that the values for B_p are about twice the line-of-sight strengths measured with the CN Zeeman effect ($B_{los} = -0.4 \text{ mG}$ for MM1 and -0.7 mG for MM2). Combining the field strengths in the plane of sky and in the line of sight, we find that the magnetic fields in MM1 and MM2 are pointed toward us and have an angle $\sim 30^\circ$ to the plane of the sky. Although the CO dispersion is probably not probing the same part of the magnetic field as the CN Zeeman data, our estimate of the total field strength could be useful because the field morphology seems to be fairly uniform throughout the envelope and the cores (§3.3).

4.3. Apparent Anomalies in Dust Polarization

Our dust polarization detections are patchy in DR21(OH). As discussed in §4.1, if the polarization in the northern patch follows the prediction for the magnetic alignment, it will be difficult to construct a smooth magnetic field geometry. There is also a large polarization gap northwest of the peaks of the double cores and south of the polarized region in the northern edge of the cores (Fig. 1). The relation between the polarization percentage and the total intensity derived in §3.1 and shown in Fig. 3 fails in this polarization gap, suggesting that there are some physical parameters controlling the degree of polarization other than the magnetic alignment efficiency of the dust grains.

We discuss several possible solutions for these apparent anomalies in dust polarization. (1) A twisted field structure could cause low polarization; however, the smooth distribution of the CO polarization contradicts this explanation. (2) If the magnetic field direction is almost parallel to the line of sight, slight variation in the field direction can result in the different angles for polarizations; however, this is not consistent with the magnetic field direction we derived in §4.2 unless the CF formula is inadequate for estimates of the field strengths. (3) It is possible that the dust polarization in the northern edge originates from dust alignment mechanisms that can produce polarization angles parallel to the field directions, such as the Gold alignment caused by strong gas streams (Gold 1952; Lazarian 1994, 1997). The change

of the alignment mechanism has been suggested to be responsible for the abrupt polarization angles changes in the Orion-KL region (Rao et al. 1998). If there are unseen outflows (i.e. that show up at radial velocities lower than 25 km s^{-1} relative to the systematic velocity), the combination of the mechanical alignment and the magnetic alignment of the dust grains could produce the polarization gap as these two effects generate orthogonal polarization. (4) The dust polarization detections at the northern edge could originate from an additional source along the line of sight. The gap can therefore be produced by the cancellation of orthogonal polarization. More sensitive dust polarization data and kinematic information are needed to examine these four possibilities.

4.4. Outflows and Magnetic fields

In Figure 7, we overlaid the CO outflows on the inferred magnetic field directions from CO and dust polarizations (assuming the dust is aligned by magnetic fields). The outflows seem to follow the field directions near MM1 and MM2, but depart from the field directions away from the two cores. These results seem to be contrary the theoretical expectations that the outflows are collimated or bent by magnetic fields (Shu et al. 1995; Hurka, Schmid-Burgk, & Hardee 1999). However, the scales at which the outflow are collimated, $\sim 1 \text{ AU}$ (Shu et al. 1995), are much smaller than that traced with the BIMA angular resolution. In addition, the CO polarization and the high-velocity outflows are detected in different velocity ranges; the CO polarization detection is associated with the -10 km s^{-1} peak, which is between the ambient velocity and the velocity of the blue lobe. It is possible that the outflows have escaped from the cores, so the field direction in the cores cannot be used to represent that in the outflows. A proper comparison between the outflows and the magnetic field is better made with the detection of CO polarization in the outflow velocity range.

5. Conclusion

We have measured linear polarization of the thermal dust emission at $\lambda \sim 1.3 \text{ mm}$ and the CO $J=2 \rightarrow 1$ emission toward DR21(OH).

- The CO polarization is approximately perpendicular to the dust polarization associated with MM1 and MM2 and parallel to the dust polarization in the northern edge of the cores, which is consistent with the predictions of the Goldreich-Kylafis effect.
- The extended CO polarization of DR21(OH) provides a better presentation of the field

morphology in DR21(OH) in the plane of the sky, which is approximately parallel to the long axis of the double cores.

- The plane-of-sky magnetic field strength B_p estimated from the Chandrasekhar-Fermi formula is ~ 0.9 mG for MM1 and ~ 1.3 mG for MM2. Combined with the previous CN Zeeman measurements, we find the magnetic field directions of MM1 and MM2 in 3-D space are both pointed toward us and have an angle $\sim 30^\circ$ to the plane of the sky.
- Our CO data provide the first maps of the high-velocity outflows originating from MM1 and MM2. The outflow direction in the downstream disagrees with the field direction of the cores, suggesting that the outflows have escaped the cores to the extent that the core magnetic field is not relevant to the outflows.

This research was supported by NSF grants AST 99-81363 and 02-05810. J. M. G. acknowledges support by MCyT grant AYA-2002-00205.

REFERENCES

- Batrla, W., & Menten, K. M. 1988, ApJ, 329, L117
- Campbell, M. F., Niles, D., Nawfel, R., Hawrylycz, M., Hoffmann, W. F., & Thronson, H. A. 1982, ApJ, 261, 550
- Crutcher, R. M., Troland, T. H., Lazareff, B., Paubert, G. & Kazès, I. 1999, ApJL, 514, L121
- Dotson, J. L., Davidson, J., Dowell, C. D., Schleuning, D. A., & Hildebrand, R. H. 2000, ApJS, 128, 335
- Downes, D., & Rinehart, R. 1966, ApJ, 144, 937
- Fischer, J., Sanders, D. B., Simon, M., & Solomon, P. M. 1985, ApJ, 293, 508
- Forster, J. R., Welch, W. J., Wright, M. C. H., & Baudry, A. 1978, ApJ, 221, 137
- Girart, J. M., Crutcher, R. M., & Rao, R. 1999, ApJ, 525, 109
- Genzel, R., & Downes, D. 1977, A&AS, 30, 145
- Goldreich, P., Kylafis, N. D. 1981, ApJ, 243, 75

- Goldreich, P., Kylafis, N. D. 1982, *ApJ*, 253, 606
- Greaves, J. S., Holland, W. S., Minchin, N. R., Murray, A. G., & Stevens, J. A. 1999a, *A&A*, 344, 668
- Greaves, J. S., Holland, W. S., Friberg, P., & Dent, W. R. F. 1999b, *ApJ*, 512, L139
- Gold, T. 1952 *MNRAS*, 112, 215
- Harvey, J. A., Ruderman, M. A., & Shaham, J. 1986, *Phys. Rev. D*, 33, 2084
- Hurka, J. D., Schmid-Burgk, J., & Hardee, P. E. 1999, *A&A*, 343, 558
- Johnston, K. J., Henkel, C., & Wilson, T. L. 1984, *ApJ*, 285, L85
- Kylafis, N. D. 1983, *ApJ*, 267, 137
- Lai, S.-P., Crutcher, R. M., Girart, J. M., & Rao, R. 2001, *ApJ*, 561, 864 (Paper I)
- Lai, S.-P., Crutcher, R. M., Girart, J. M., & Rao, R. 2002, *ApJ*, 566, 925 (Paper II)
- Lazarian, A. 1994, *MNRAS*, 268, 713
- Lazarian, A. 1997, *ApJ*, 483, 296
- Lee, C., Mundy, L. G., Reipurth, B., Ostriker, E. C., & Stone, J. M. 2000, *ApJ*, 542, 925
- Mangum, J. G., Wootten, A., & Mundy, L. G. 1992, *ApJ*, 388, 467
- Matthews, B. C. & Wilson, C. D. 2002, *ApJ*, 574, 822
- Norris, R. P., Booth, R. S., Diamond, P. J., & Porter, N. D. 1982, *MNRAS*, 201, 191
- Padin, S. et al. 1989, *ApJ*, 337, L45
- Plambeck, R. L., & Menten, K. M. 1990, *ApJ*, 364, 555
- Richardson, K. J., Sandell, G., Cunningham, C. T., & Davies, S. R. 1994, *A&A*, 286, 555
- Rao, R., Crutcher, R. M., Plambeck, R. L., & Wright, M. C. H. 1998, *ApJ*, 502, L75
- Shu, F. H., Najita, J., Ostriker, E. C., & Shang, H. 1995, *ApJ*, 455, L155
- Ward-Thompson, D., Kirk, J. M., Crutcher, R. M., Greaves, J. S., Holland, W. S., & André, P. 2000, *ApJ*, 537, L135

Woody, D. P., Scott, S. L., Scoville, N. Z., Mundy, L. G., Sargent, A. I., Padin, S., Tinney, C. G., & Wilson, C. D. 1989, ApJ, 337, L41

Table 1: Polarization measurements in DR21(OH)

Offsets ^a ($''$, $''$)	Dust		CO		Note
	P (%)	ϕ ($^\circ$)	P (%)	ϕ ($^\circ$)	
(-2.2,-6.0)	9.0 \pm 3.2	-17 \pm 10			
(-3.8,-6.0)	12.1 \pm 3.9	-10 \pm 9			
(5.8,-4.0)	12.9 \pm 3.6	-59 \pm 8			
(-0.6,-4.0)			0.7 \pm 0.2	50 \pm 9	
(-2.2,-4.0)	4.0 \pm 1.1	-27 \pm 8	0.9 \pm 0.2	50 \pm 8	
(-3.8,-4.0)	6.8 \pm 1.3	-23 \pm 6	0.7 \pm 0.2	48 \pm 9	polarization peak near MM2
(-5.4,-4.0)	7.1 \pm 2.2	-16 \pm 9			
(12.2,-2.0)			1.2 \pm 0.4	-86 \pm 10	
(7.4,-2.0)	7.5 \pm 2.6	-40 \pm 10			
(5.8,-2.0)	6.6 \pm 1.7	-54 \pm 7			
(4.2,-2.0)	6.1 \pm 1.4	-48 \pm 6			
(2.6,-2.0)	6.3 \pm 1.3	-47 \pm 6			polarization peak near MM1
(1.0,-2.0)			0.6 \pm 0.2	61 \pm 7	
(-0.6,-2.0)	2.9 \pm 0.8	-30 \pm 8	0.9 \pm 0.2	60 \pm 5	
(-2.2,-2.0)	3.0 \pm 0.6	-29 \pm 6	0.9 \pm 0.2	57 \pm 5	
(-3.8,-2.0)	3.5 \pm 0.7	-23 \pm 6	0.8 \pm 0.2	58 \pm 6	
(-5.4,-2.0)	4.4 \pm 1.2	- 7 \pm 8	0.6 \pm 0.2	69 \pm 8	
(12.2, 0.0)			1.0 \pm 0.3	-70 \pm 8	
(10.6, 0.0)			0.7 \pm 0.3	-75 \pm 10	
(5.8, 0.0)			0.7 \pm 0.2	84 \pm 8	
(4.2, 0.0)	2.6 \pm 0.7	-50 \pm 8	0.7 \pm 0.2	85 \pm 7	
(2.6, 0.0)	2.8 \pm 0.7	-51 \pm 7	0.6 \pm 0.1	80 \pm 7	
(1.0, 0.0)	2.5 \pm 0.9	-33 \pm 10	0.7 \pm 0.1	71 \pm 5	
(-0.6, 0.0)	2.8 \pm 0.7	-20 \pm 7	1.0 \pm 0.1	69 \pm 4	
(-2.2, 0.0)	2.1 \pm 0.6	-21 \pm 8	1.0 \pm 0.1	68 \pm 4	MM2 peak
(-3.8, 0.0)	2.1 \pm 0.6	-10 \pm 9	0.9 \pm 0.1	68 \pm 5	
(-5.4, 0.0)	3.2 \pm 1.0	6 \pm 9	0.8 \pm 0.2	68 \pm 6	
(-7.0, 0.0)			0.6 \pm 0.2	66 \pm 10	
(12.2, 2.0)			1.1 \pm 0.2	-65 \pm 6	
(10.6, 2.0)			1.0 \pm 0.2	-70 \pm 6	
(9.0, 2.0)			0.8 \pm 0.2	-76 \pm 7	
(7.4, 2.0)			0.8 \pm 0.2	-80 \pm 7	
(5.8, 2.0)			0.7 \pm 0.2	-85 \pm 6	
(4.2, 2.0)	1.7 \pm 0.4	-57 \pm 7	0.7 \pm 0.1	89 \pm 6	MM 1 peak
(2.6, 2.0)			0.7 \pm 0.1	84 \pm 6	
(1.0, 2.0)			0.8 \pm 0.1	78 \pm 5	
(-0.6, 2.0)			0.9 \pm 0.1	77 \pm 5	
(-2.2, 2.0)			0.9 \pm 0.1	77 \pm 4	
(-3.8, 2.0)			0.9 \pm 0.2	74 \pm 5	
(-5.4, 2.0)			0.8 \pm 0.2	68 \pm 6	
(-7.0, 2.0)			0.6 \pm 0.2	61 \pm 9	
(13.8, 4.0)			1.1 \pm 0.3	-52 \pm 8	
(12.2, 4.0)			1.5 \pm 0.3	-60 \pm 5	
(10.6, 4.0)			1.4 \pm 0.2	-65 \pm 5	
(9.0, 4.0)			1.1 \pm 0.2	-71 \pm 5	
(7.4, 4.0)	4.3 \pm 1.1	-10 \pm 7	0.9 \pm 0.2	-77 \pm 6	
(5.8, 4.0)	1.9 \pm 0.6	-12 \pm 8	0.8 \pm 0.2	-86 \pm 7	
(4.2, 4.0)			0.7 \pm 0.2	87 \pm 7	
(2.6, 4.0)			0.7 \pm 0.2	85 \pm 6	
(1.0, 4.0)			0.7 \pm 0.2	83 \pm 7	
(-0.6, 4.0)			0.7 \pm 0.2	84 \pm 7	
(-2.2, 4.0)			0.7 \pm 0.2	85 \pm 6	
(-3.8, 4.0)			0.8 \pm 0.2	81 \pm 6	
(-5.4, 4.0)			0.7 \pm 0.2	75 \pm 8	
(15.4, 6.0)			1.7 \pm 0.6	-41 \pm 10	
(13.8, 6.0)			2.1 \pm 0.4	-49 \pm 6	
(12.2, 6.0)			2.3 \pm 0.4	-53 \pm 4	
(10.6, 6.0)			2.1 \pm 0.3	-55 \pm 4	
(9.0, 6.0)	9.6 \pm 3.1	- 6 \pm 9	1.6 \pm 0.3	-60 \pm 5	
(7.4, 6.0)	4.4 \pm 1.4	-10 \pm 9	1.1 \pm 0.2	-70 \pm 6	
(5.8, 6.0)			0.7 \pm 0.2	-85 \pm 8	
(4.2, 6.0)			0.7 \pm 0.2	88 \pm 8	
(2.6, 6.0)			0.6 \pm 0.2	87 \pm 8	
(-0.6, 6.0)	8.4 \pm 2.6	-93 \pm 9			northern region
(-2.2, 6.0)	11.7 \pm 3.0	-80 \pm 7	0.6 \pm 0.2	-90 \pm 10	northern region
(9.0, 8.0)			2.4 \pm 0.6	-50 \pm 7	
(7.4, 8.0)			1.4 \pm 0.4	-62 \pm 8	
(5.8, 8.0)			0.8 \pm 0.2	-76 \pm 9	
(-0.6, 8.0)	18.0 \pm 6.0	-90 \pm 9			northern region
(-2.2, 8.0)	22.3 \pm 5.8	-84 \pm 7			northern region
(-2.2,10.0)	36.4 \pm 11.2	-104 \pm 7			northern region

^aOffsets are measured with respect to the phase center: $\alpha_{2000}=20^h39^m00^s.72$, $\delta_{2000}=42^\circ22'46''.7$.

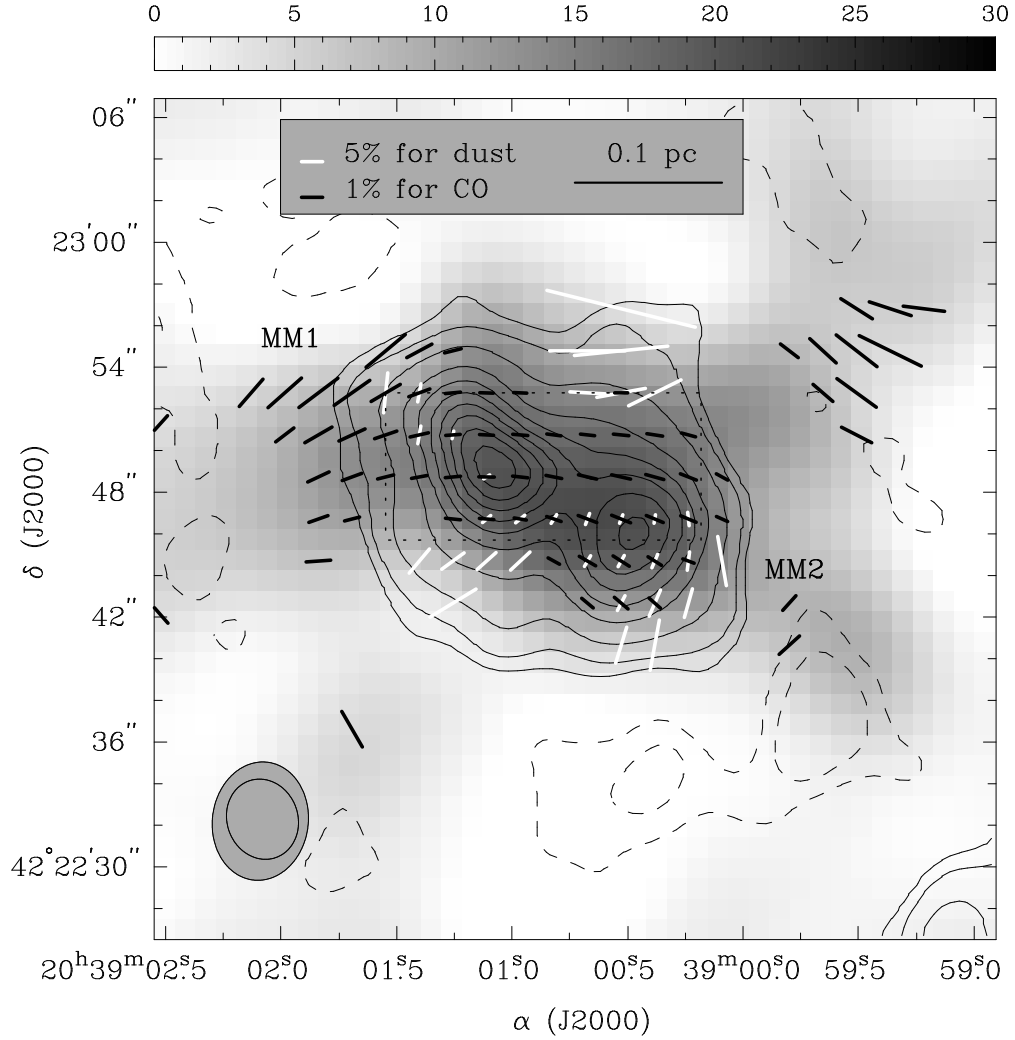


Fig. 1.— Polarization map of DR21(OH). The contours show the Stokes I of the dust continuum at -30 , -18 , 18 , 30 , 60 , 120 , 180 , 240 , 300 , 360 , 420 , and $480 \text{ mJy beam}^{-1}$. The grey-scale shows the Stokes I of the CO $J=2 \rightarrow 1$ emission with v_{LSR} of -10 km s^{-1} , $\Delta v = 11.5 \text{ km s}^{-1}$. The grey-scale bar on the top is in units of $\text{Jy beam}^{-1} \text{ km s}^{-1}$. The synthesized beam size is $3''.9 \times 3''.4$ with $\text{PA} = 19^\circ$ for the dust continuum and $5''.7 \times 4''.6$ with $\text{PA} = -7^\circ$ for CO, which are shown with grey ellipses. The white and black line segments represent the dust and CO polarization vectors with a scale of 5% and 1% per arcsecond length, respectively. The dashed rectangle includes the region associated with the peak of the polarized CO $J=2 \rightarrow 1$ emission, and the Stokes I , Q , and U spectra integrated over this rectangle are shown in Fig. 4.

Table 2: Summary of analysis in polarization angle

Region	Tracer	Average	Observed	Measurement	Intrinsic
		Angle $\phi(^{\circ})$	Dispersion $\delta\phi_{obs}(^{\circ})$	Uncertainty $\sigma_{\phi}(^{\circ})$	Dispersion $\delta\phi_{int}(^{\circ})$
MM1 and MM2	Dust	-27	21 ± 7	7.6 ± 1.2	20 ± 7
CO pol Main	CO	89	23 ± 5	6.3 ± 1.6	22 ± 5

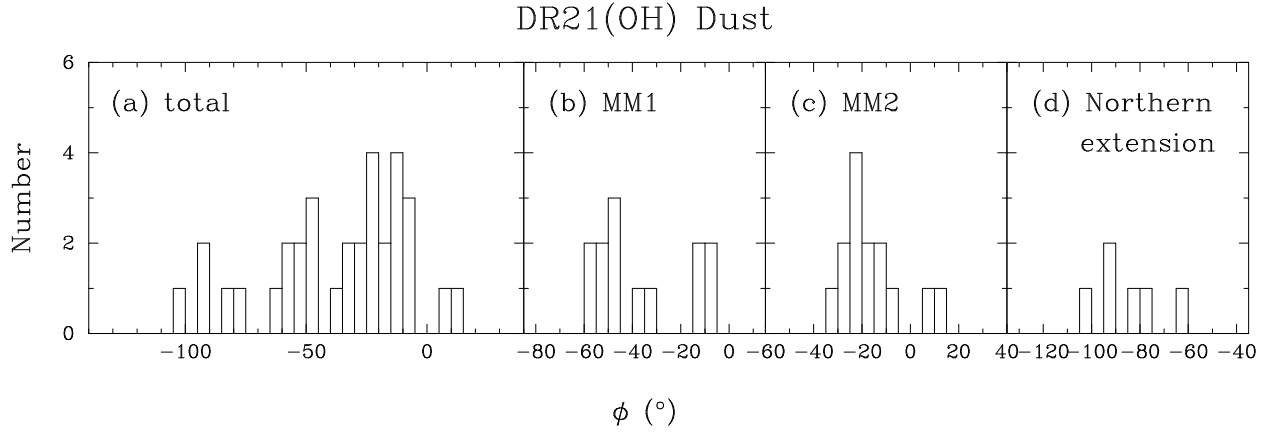


Fig. 2.— Polarization angle distribution of the dust continuum of DR21(OH). (a) shows the histogram of all dust polarization measurements in DR21(OH). (b)-(d) shows dust polarization measurements of DR21(OH) in three separate regions. The vertical axes for these plots are the total number of the measurements in the bin.

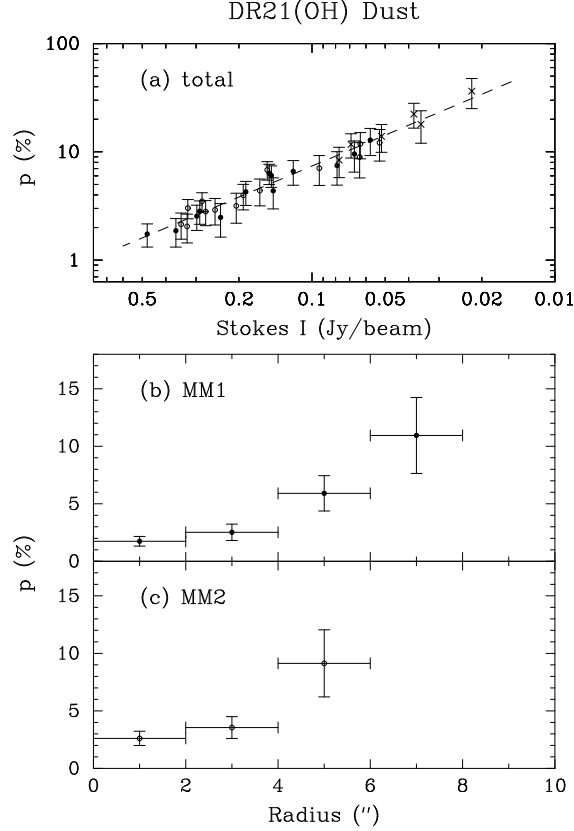


Fig. 3.— Polarization percentage distribution of the dust continuum of DR21(OH). The filled dots represent the data associated with MM1, the open dots represent the data associated with MM2, and the crosses represent the data in the northern edge of the two cores. The dotted line is the best least-squares fit for the data. (a) shows the polarization percentage vs. the total intensity. The error bar of each data point is the measurement error. The total intensity increases to the left in order to emphasize that high intensity corresponds to short distance to the center of the cores. (b) and (c) show the polarization percentage vs. the distance from MM1 and MM2. The error bar in radius shows the range over which the data are averaged and the error bar in p is the standard deviation of the data in the range.

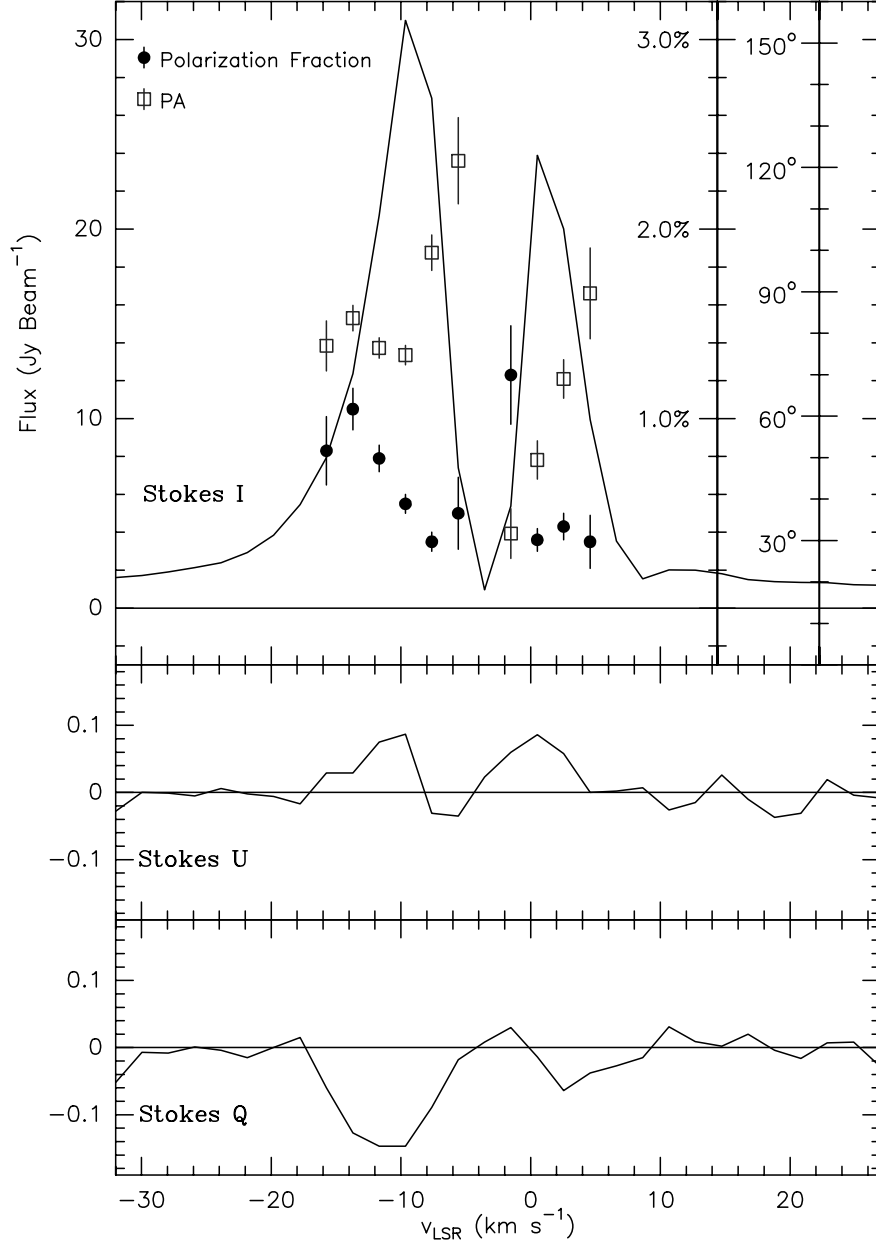


Fig. 4.— CO $J=2 \rightarrow 1$ polarization spectra of DR21(OH). The Stokes I , Q , and U spectra were integrated over the dashed rectangle in Fig. 1.

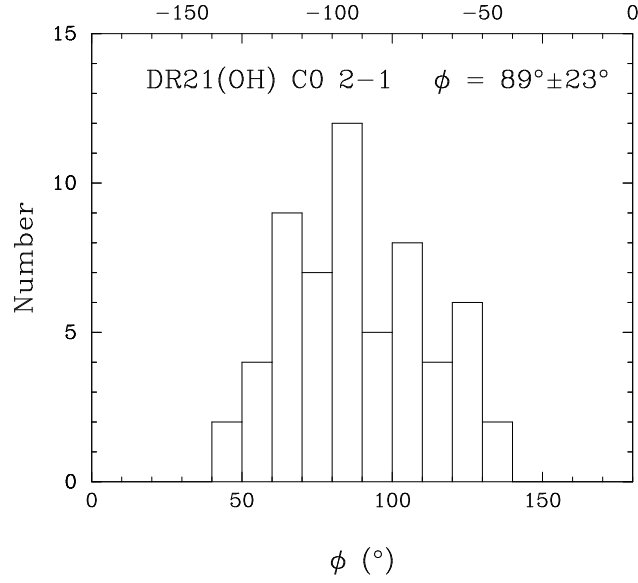


Fig. 5.— Polarization angle distribution of the CO $J=2 \rightarrow 1$ emission of DR21(OH) associated with the dust continuum (CO pol Main). For easy comparison with the dust polarization, we label $\phi - 180^\circ$ on the top of the plot. For polarization “vectors”, $\phi - 180^\circ$ is equivalent to ϕ . The vertical axis is the total number of the measurements in the bin.

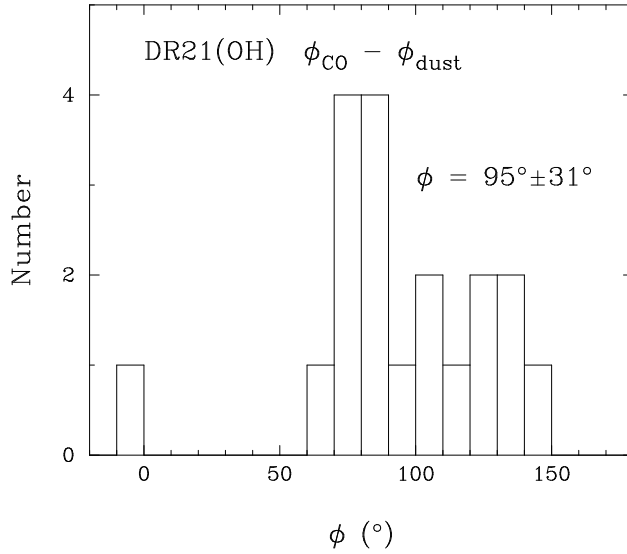


Fig. 6.— Polarization angle distribution of the difference between CO and dust polarization in DR21(OH). The vertical axis is the total number of the measurements in the bin. The average angle and dispersion (excluding the data point around 0°) is labeled in the plot.

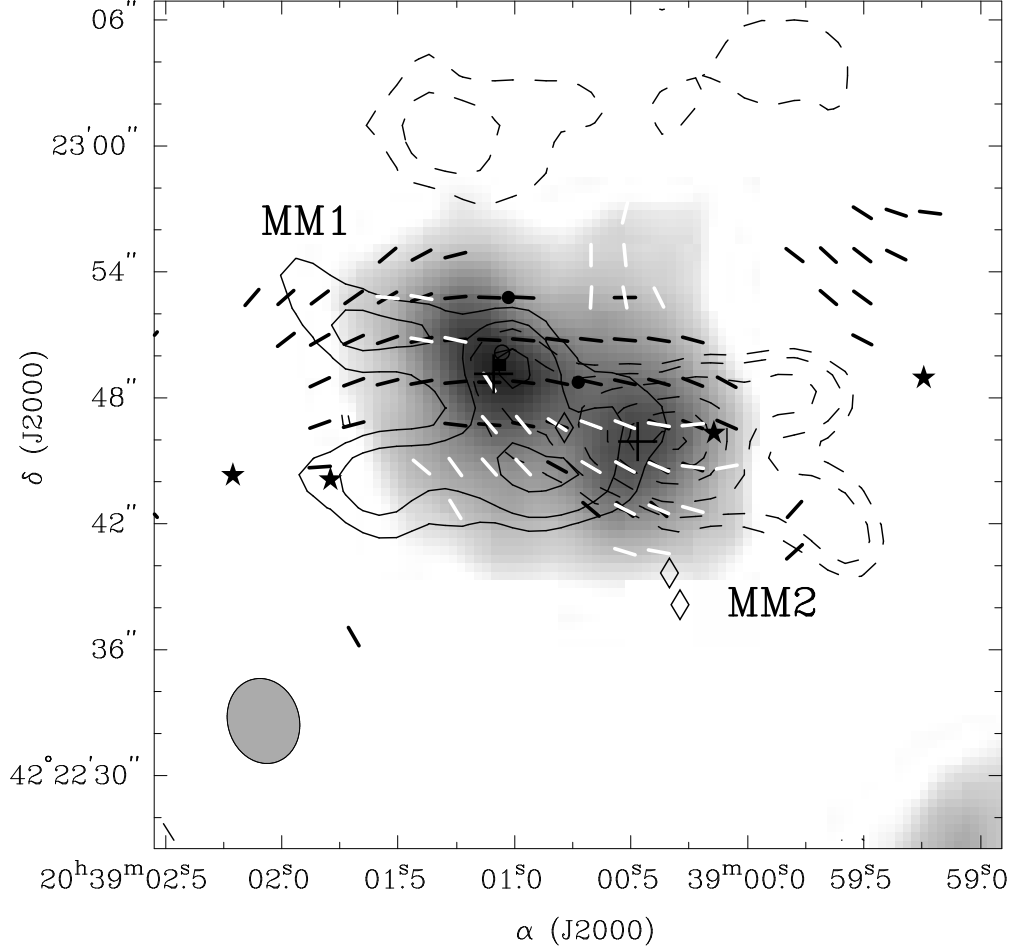


Fig. 7.— The high-velocity outflows in DR21(OH). The dashed and solid contours represent the blue and red lobes of CO $J=2 \rightarrow 1$ outflows at the velocity of -30 and 20 km s^{-1} integrated over 7 km s^{-1} bandwidths. The beamsize is $4''.1 \times 3''.4$ with $\text{PA}=16^\circ$. The grey-scale shows the dust continuum at 1.3 mm and the peaks of MM1 and MM2 are marked by plusses. The black and white line segments indicate the magnetic field direction inferred from the CO and dust polarization (assuming the dust is aligned by magnetic fields). The various symbols indicate the maser positions: stars denote methanol masers (Plambeck & Menten 1990; filled square represents the OH maser (Norris et al. 1982); filled circles, open circles, and open diamonds are water masers observed at different epochs (Genzel & Downes 1977; Forster et al. 1978; Mangum, Wootten, & Mundy 1992).